Diagnosing Potts criticality and two-stage melting in one-dimensional hard-boson models

G. Giudici*, ^{1, 2, 3} A. Angelone*, ^{1, 2} G. Magnifico, ^{1, 4, 5} Z. Zeng, ⁶ G. Giudice, ⁷ T. Mendes-Santos, ¹ and M. Dalmonte^{1, 2}

¹ The Abdus Salam International Centre for Theoretical Physics, strada Costiera 11, 34151 Trieste, Italy

² SISSA, via Bonomea 265, 34136 Trieste, Italy

³ INFN, via Bonomea 265, 34136 Trieste, Italy

⁴ Dipartimento di Fisica e Astronomia dell'Università di Bologna, I-40127 Bologna, Italy

⁵ INFN, Sezione di Bologna, I-40127 Bologna, Italy

⁶ School of Physics, Sun Yat-sen University, Guangzhou 510275, China.

⁷ Max-Planck Institute of Quantum Optics, Hans-Kopfermann-Str. 1, 85748 Garching, Germany

(Dated: 17th December 2022)

We investigate a model of hard-core bosons with infinitely repulsive nearest- and next-nearest-neighbor interactions in one dimension, introduced by Fendley, Sengupta and Sachdev in Phys. Rev. B 69, 075106 (2004). Using a combination of exact diagonalization, tensor network, and quantum Monte Carlo simulations, we show how an intermediate incommensurate phase separates a crystalline and a disordered phase. We base our analysis on a variety of diagnostics, including entanglement measures, fidelity susceptibility, correlation functions, and spectral properties. According to theoretical expectations, the disordered-to-incommensurate-phase transition point is compatible with Berezinskii-Kosterlitz-Thouless universal behaviour. The second transition is instead non-relativistic, with dynamical critical exponent z>1. For the sake of comparison, we illustrate how some of the techniques applied here work at the Potts critical point present in the phase diagram of the model for finite next-nearest-neighbor repulsion. This latter application also allows to quantitatively estimate which system sizes are needed to match the conformal field theory spectra with experiments performing level spectroscopy.

I. INTRODUCTION

Recent years have witnessed a considerable experimental progress aimed at realizing and manipulating atomic physics systems with long-range interactions^{1,2}. Examples of this span a variety of platforms, including trapped ions³, cold polar molecules⁴, and atomic gases of strongly dipolar atoms such as Cr, Dy, and Er¹. Strong non-local interactions can also be induced on neutral atoms by coupling their atomic ground states to Rydberg states^{5–9}. The large dipole moments displayed by the latter allow to engineer large dipolar and van-der-Waals interactions^{10–15}, which offer the possibility of performing quantum simulation of long-range, strongly interacting systems¹⁶.

These new avenues of experimental realization have caused renewed interest in many theoretical models which, besides displaying remarkable physical phenomena, might be realized within present experimental settings. In this work, we will focus on one such model, first introduced in Ref. 17 by Fendley, Sengupta and Sachdev (FSS). The model describes an array of one-dimensional strongly interacting hard-core bosons in the presence of occupation constraints on nearest-neighbor (NN), and with additional interactions on next-to-nearest-neighbor (NNN), sites. Initially discussed due to its connections with integrable models, its successful implementation in Rydberg atom arrays¹¹ has driven further theoretical investigation 18–22.

The phase diagram of the FSS model displays a variety of phases and phase transitions which still needs to be fully understood (see Fig. 1). In particular, there are

two ordered phases with \mathbb{Z}_2 and \mathbb{Z}_3 order¹⁷ and a disordered phase in which long-range correlations can be incommensurate with the lattice spacing²⁰. The transition separating the period-two ordered phase from the disordered one is well understood: one switches from first to second order at a tricritical point, the second order line belonging to the Ising model universality class²³. The phase diagram hosts an integrable line, which crosses the boundary between the \mathbb{Z}_3 -ordered and disordered phases at a critical point belonging to the Potts universality class^{23,24}. Below it, the phase transition is still continuous, but Lorentz invariance is broken at low energy by an irrelevant chiral perturbation which changes the critical exponents^{20,25}. Eventually, a gapless phase opens on the line and the order-disorder transition becomes a Luttinger liquid phase^{23,26} with incommensurate long-range correlations 17,20 .

Above the Potts critical point the situation is more controversial, and so far several scenarios have been proposed. The chiral perturbation *i*) might become relevant, making the transition first order; *ii*) it might lead to the same effect as below the Potts point, thus leaving the transition continuous; or *iii*) it might stabilize an intervening gapless phase between the ordered and disordered phase. In principle, the transition may remain in the Potts universality class: however, this scenario is unlikely as it would require fine-tuning. Recently, numerical evidence has been provided both in favor of a continuous phase transition surviving on the whole line 19 and in favor of a gapless phase opening at a point above the Potts one 20, while simulations on small system sizes are compatible with Potts universality extending up to infinite

NNN repulsion 18 .

The aim of this paper is to clarify the nature of the \mathbb{Z}_3 -order-to-disorder transition above the integrable line. We focus on the regime of infinite NNN repulsion, which we refer to as *doubly-blockaded regime*, in analogy with the more common NN blockade. The reason for this choice is threefold: being it the farthest regime from the Potts critical point, it may allow for a comparatively larger incommensurate phase (if any) thanks to the fact that the role of perturbations moving away from the exactly solvable line (see Fig. 1) is typically larger; it is of easy experimental access; it is amenable to exact simulations up to comparatively larger sizes with respect to the rest of the phase diagram.

We show that the melting of the ordered phase, at the boundary of the phase diagram, takes place via an intermediate gapless phase. This critical phase is enclosed between two continuous phase transitions. From the disordered side, the transition is of the BKT type, while from the ordered side the universality class is not captured by conformal field theory (CFT).

We compute many of the critical exponents of these transitions with different methods: as we discuss below, our findings are only able to provide a lower bound for the size of the incommensurate (IC) phase, due to the presence of anomalously large finite-size effects – small sizes systematically reduce the size of the IC phase. In parallel, we test some of the methods employed on the exactly located Potts critical point: this helps us to emphasize differences and similarities between the two melting phase transitions. We also give a full characterization of the Potts critical point by computing its critical exponents, and by matching the low-lying energy spectrum on the lattice with the universal predictions provided by conformal field theory. This characterization provides a quantitative and unambiguous testbed to verify Potts quantum criticality in experiments based on spectroscopic probes.

We employ various methods to tackle the problem numerically, focusing on periodic geometries in order to avoid boundary effects, which are particularly detrimental for constrained models in the vicinity of ordered phases. We exploit at best the small quantum dimension of the Hilbert space to compute the ground state and the lowest excited states exactly up to 54 sites. We perform studies of up to 120 sites via quantum Monte Carlo (QMC), using an imaginary-time path integral method sharing many similarities with the Worm Algorithm²⁷, adapted to simulate Hamiltonians with offdiagonal terms such as those of the FSS model and with updates designed to automatically respect its occupation constraints. We use the density matrix renormalization group (DMRG) algorithm²⁸ to compute the ground state of periodic chains up to 108 sites. In this case, we implement the constraint by giving a large penalty to the states which are not allowed in the Hilbert space. We also present results for the experimentally realized open chain scenario by simulating open chains up to 718 sites

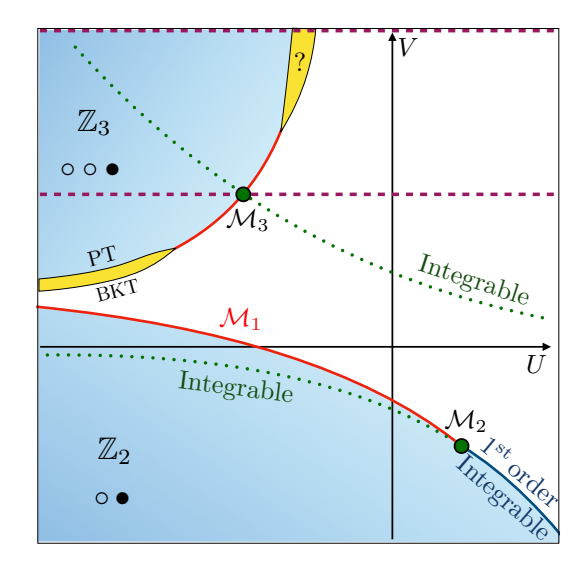


Figure 1. Phase diagram of the model Hamiltonian Eq. (1). Ordered phases are colored in light blue. Red (blue) lines indicate second (first) order phase transitions. On the green dotted lines the model is integrable. The integrable line in the lower half plane is on top of the transition line when the transition is of the first order. The two lines separate at the tricritical point \mathcal{M}_2 , where the transition becomes continuous. After this point, the second order phase transition belongs to the Ising universality class. The integrable line in the upper half plane crosses the second order transition line exactly at the \mathcal{M}_3 critical point, belonging to the Potts model universality class. Below this point, on the transition line, a gapless phase (lower yellow region, not in scale) opens, enclosed within a Pokrovsky-Talapov (PT) and Berezinskii-Kosterlitz-Thouless (BKT) transition. Above this point, the opening of a gapless phase (upper yellow region, not in scale) is under debate. Purple dashed lines are studied in this work.

with a 1-site DMRG algorithm formulated in the matrix product state (MPS) language, which allows to realize the constraint exactly by representing efficiently the global projector on the constrained Hilbert space as a matrix product operator (MPO).

The structure of the paper is as follows. In Sec. II, we present the Hamiltonian of the model, stressing its importance in relation to Rydberg atoms experiments¹¹ and reviewing in detail previous theoretical results. In Sec. III, we discuss the methods we employ, and investigate the vicinity of the Potts transition point, in particular, performing an analysis based on level spectroscopy. In Sec. IV, we study in detail the doubly-blockaded regime. In Sec. V, we draw our conclusions and discuss some future perspectives.

II. MODEL HAMILTONIAN AND REVIEW OF PREVIOUS RESULTS

A. Hard-core interactions in Rydberg-blockaded gases

Alkali atoms in Rydberg states^{6–8,29} are characterized by one of their electrons occupying an energy level with high principal quantum number (n>40). Several features of the atomic state are strongly influenced by this type of excitation. Examples include a very long radiative lifetime $\tau \sim n^3$, a large orbital radius $r_o \sim n^2$ and a strong dipole moment $d \sim n^2$: in the case of Rubidium excited to the 50p state, these quantities can assume values of the order of $10^2~\mu s$, $10^{-1}~\mu m$ and $10^3~ea_0$, respectively.

These remarkable characteristics determine the strong interactions between Rydberg atoms. The dominant contribution to the latter will be of the dipole-dipole $(V(r) \sim r^{-3})$ with the interatomic distance r or vander-Waals $(V(r) \sim r^{-6})$ type in the presence and absence of external polarizing field, respectively, due to the aforementioned strong dipole moments. The large values displayed by the latter cause these interactions to be very strong, with a typical scaling for the van-der-Waals coupling constant being $C \sim n^{11}$.

Due to their extremely high values, Rydberg–Rydberg interactions far outstrip any other energy scale in the system, and therefore play a fundamental role in determining the behavior of a many-body Rydberg ensemble. One of the most remarkable phenomena induced in this interaction-dominated picture is the Rydberg Blockade^{5,30}, in which the excited atomic levels, due to the strength of the interatomic potential V(r), are heavily shifted from their noninteracting positions. Since V(r) becomes stronger at short distances, a Rydberg atom creates an effective "exclusion zone" around itself, where no other excitations to the Rydberg state can take place (due to the excited level being too strongly off-resonance with respect to the excitation mechanism, usually a laser in experimental setups).

In a many-body system of Rydberg atoms, this phenomenon can be used to simulate an effective hard-shell constraint: gauging the experimental parameters (namely, the frequency and the detuning of the laser used to induce excitations to the Rydberg state) the blockade radius can be tuned to simulate occupancy constraints for sites at different distances on an optical lattice, reproducing the most significant feature of models such as the FSS Hamiltonian, as realized in Ref. 11.

B. Hard-boson model phase diagram

The Hamiltonian of the FSS model is given by

$$H = -\sum_{i} (d_i + d_i^{\dagger}) + U \sum_{i} n_i + V \sum_{i} n_i n_{i+2}$$
 (1)

where d_i^{\dagger} (d_i) is the creation (destruction) operator for a hard-core boson on site i and $n_i = d_i^{\dagger} d_i$. The Hilbert space is subjected to the constraint $n_i n_{i+1} = 0$, namely two particles cannot occupy NN sites. When this restriction is imposed, the number of states $\dim \mathcal{H}_L$ in the Hilbert space for a chain of length L satisfies, in the case of open boundary conditions (OBC), the recursive equation

$$\dim \mathcal{H}_L = \dim \mathcal{H}_{L-1} + \dim \mathcal{H}_{L-2} \tag{2}$$

whose solution is the Fibonacci sequence, which behaves asymptotically for large L as $\dim \mathcal{H}_L \sim \phi^L$, where $\phi = 1.6180...$ is the Golden ratio. The dimension of \mathcal{H} becomes even smaller in the limit $V \to \infty$, which is equivalent to say that there have to be at least two empty lattice sites between two particles, i.e. $n_i n_{i+1} = 0$ and $n_i n_{i+2} = 0$. It is easy to see that in this case $\dim \mathcal{H}_L$ satisfies the equation

$$\dim \mathcal{H}_L = \dim \mathcal{H}_{L-1} + \dim \mathcal{H}_{L-3} \tag{3}$$

which asymptotically means $\dim \mathcal{H}_L \sim \zeta^L$, with $\zeta = 1.4655$

The model was first proposed as the quantum version of the 2-dimensional classical hard-square model¹⁷, which is known to host two integrable lines³¹. One of the two lines crosses the period-three-to-disorder line exactly at the Potts critical point, whose location is thus known analytically. The classical-to-quantum mapping results in a constrained quantum Hilbert space which is not in product form. As already noted in Ref. 20 and further discussed below, the peculiar way order is realized in the system causes extremely strong finite-size effects, especially when OBC are applied. This poses challenges for tensor-network based techniques, which usually rely on these boundary conditions, since the computational effort must be increased in order to access larger system sizes. Oppositely, the milder scaling of the Hilbert space dimension allows to exactly diagonalize the system up to lengths which roughly double the usual lengths accessible in spin chains. Since periodic boundary conditions (PBC) eliminate boundary effects, in addition to providing momentum symmetry for a direct diagonalization of the quantum Hamiltonian, they will be employed throughout this work, with the exception of the tensor network simulations presented in Sec. IV.

The phase diagram of the model is depicted in Fig. 1. The two integrable lines are parametrized by

$$V(U+V) = 1. (4)$$

One of the two lines is defined on the upper-half-plane (U,V), and crosses the order-disorder transition line exactly at the Potts critical point mentioned above, for $V = V_c = [(\sqrt{5} + 1)/2]^{5/2}$; it is thus described at low energies by the third conformal field theory in the minimal series, \mathcal{M}_3^{23} . The gapped ordered phase extends to a region in the quadrant V > 0, U < 0, where the order-disorder transition is not always a sharp transition. In

particular, it was shown in Ref. 17 that in the limit case $U \to -\infty$ and V = -U/3 the separation line is in fact a thin gapless phase (vellow region in Fig. 1) characterized by the Luttinger liquid (LL) universality class. The transition from the ordered phase to the gapless phase belongs to the Pokrovsky-Talapov (PT) universality class³². and has dynamical critical exponent z=2. Conformal invariance is then restored in the continuum description and the transition from the gapless phase to the disordered phase is of the Berezinskii-Kosterlitz-Thouless type²⁶. Moreover, a recent detailed analysis²⁰ exhibited strong numerical evidence that the very same picture persists on the order-disorder transition line, up to a Lifshitz point located below the integrable line, beyond which the transition is sharp and of the chiral Huse-Fisher type²⁵. However, the precise location of the Lifshitz point could not be estimated. The authors also confirmed the position and nature of the Potts critical point by computing the correlation length critical exponent ν coming from both phases.

What happens above the integrable line is more controversial. A DMRG-OBC study²⁰ is in favor of a chiral transition up to another Lifshitz point after which a LL phase opens again, with a PT transition on the ordered side and a BKT transition on the disordered side. The width of the intervening LL phase was estimated at the order of 0.001. It was also noted that, above the Potts point, boundary effects are sizeable at system sizes of the order of several hundred sites, as testified by an anomalous scaling of the von Neumann entropy. Instead, an ED study¹⁹, using PBC, indicated that there is no Lifshitz point, and the transition remains chiral up to $V = \infty$, with a dynamical critical exponent $1 < z \lesssim 1.33$.

In what follows we will focus on two lines at constant V (purple dashed lines in Fig. 1). The phase diagram on the first line is very well understood and we will use it as a benchmark to test field theory predictions in this exotic quantum chain. The second line is located at $V=\infty$ and, as discussed above, its phase structure is still under debate.

III. POTTS CRITICAL POINT

In this section, we study the finite-size properties of the Potts critical point. This is important not only to test some of the methods we are going to employ in the following sections, but also to understand which universal properties can be experimentally measured with the available setups of $\simeq 50$ spins. Moreover, it is of theoretical interest, as there are very few lattice realizations of Potts criticality that can be studied in such a systematic fashion $^{33-35}$.

The CFT behind the Potts model universality class is one of the modular invariant realizations of the third model in the minimal series: \mathcal{M}_3^{36} . Its central charge is 4/5 and the most relevant primary fields, namely the energy density and the order parameter, carry anomalous

dimensions $\eta_{\varepsilon} = 4/5$ and $\eta_{\sigma} = 4/15$. These two numbers imply that the correlation length and order parameter critical exponents are $\nu = (2 - \eta_{\varepsilon})^{-1} = 5/6$ and $\beta = \nu \eta_{\sigma}/2 = 1/9$.

The position of the Potts critical point in the phase diagram of the quantum Hamiltonian in Eq. (1) is known exactly by integrability arguments 17 and its location has been checked numerically both via gap scaling analysis 19 as well as from vanishing inverse correlation length 20 . Its critical exponents have been computed on the lattice, and a clear signature of the underlying CFT has been observed 17,19,20 . However, the low-energy spectrum of the lattice Hamiltonian has never been matched with the CFT one and a full characterization of the phase transition has never been given. Furthermore, contrary to the lattice Potts model, the \mathbb{Z}_3 symmetry is not an exact global symmetry of the FSS model. It is thus non-trivial to identify the whole operator content from the energy eigenvalues on the lattice.

Before performing level spectroscopy, we test some of the methods we will employ in the next section to witness second order phase transitions without any assumption on the spacetime symmetry of the underlying field theory, namely non-analyticity in the quantum concurrence^{37,38} — which is a measure of single spin entanglement — as well as in the fidelity susceptibility^{39,40}. The latter also allows to extract the critical exponent ν of the ordered phase $^{41-43}$. We then compute the central charge of the CFT from the logarithmic scaling of the entanglement entropy⁴⁴ and we show that the CFT regime is reached with system sizes accessible to present experiments. We proceed by matching momentum symmetry sectors on the lattice with \mathbb{Z}_3 sectors in the CFT. We match several lowlying eigenvalues with the corresponding primary fields and we discuss the finite-size scaling corrections w.r.t. CFT predictions. Finally, we extract the anomalous dimension η_{σ} of the order parameter by comparing its lattice two-point function with the one of a CFT on a ring 23 .

A. Critical point location

As we will see below, in order to locate the critical point, it is useful to utilize a procedure which is not biased by any assumption on the nature of the phase transition, such as conformal invariance and a consequent scaling of the gap with a dynamical critical exponent z=1. Here we use two methods based on the non-analytic behavior displayed by generic functions in the presence of continuous phase transitions. The concurrence is a measure of entanglement for spin systems 38,45 , and is defined as

$$C = \max(0, \lambda_1 - \lambda_2 - \lambda_3 - \lambda_4) \tag{5}$$

where the λ_i are the square roots of the eigenvalues in decreasing order of the matrix $\sqrt{\rho_{i,j}}(\sigma^y \otimes \sigma^y)\rho_{i,j}^*(\sigma^y \otimes \sigma^y)\sqrt{\rho_{i,j}}$, where $\rho_{i,j}$ is the reduced density matrix of two sites located at positions i and j (here we show results

for j=i+2).⁴⁶. The function C(U) is expected to have infinite derivative at a gapless critical point in the thermodynamic limit^{37,38}. At finite size, the derivative $\partial_U C$ has a peak which sharpens with increasing system size at a value $U^*(L)$ which converges to the critical point when $L \to \infty$.

In Fig. 2(a), we plot the value of the position of the peak of $\partial_U C$, $U^*(L)$, at the Potts critical point as a function of 1/L. The position of the critical point at $L \to \infty$, U_c , is obtained by fitting $U^*(L)$ with the power-law function, $U^*(L) = U_c + A/L^{\gamma}$. The best fitting exponent for system sizes from 24 to 36 sites is $\gamma = 4.0 \pm 0.1$ and the extracted position of the critical point is $U_c = -3.03 \pm 0.04$, in good agreement with the exact value $U_c = 3.0299...$ Note however, that the result is not stable when smaller system sizes are included in the fit. We attribute this instability to the limited number of sizes we can reliably simulate in the scaling regime, due to the challenging nature of the calculation of concurrency.

Another quantity that is used to locate and characterize the critical point is the fidelity susceptibility

$$\chi_F = \frac{-2\log|\langle\psi_0(U)|\psi_0(U+\delta U)\rangle|}{\delta U^2}$$
 (6)

where $|\psi_0(U)\rangle$ is the ground state wave function for a fixed value of U. As the derivative of the concurrence, χ_F exhibits a peak at the position $U^*(L)$, when plotted as a function of U. The size scaling of $U^*(L)$ provides an alternative approach to establish the position of the critical point, U_c , see Fig. 2(b). In contrast to the concurrence, the numerical calculation of the fidelity is less expensive and allows us to reach system sizes up to L = 42. This yields a best fitting result which is stable against the range of system sizes included in the fit for $L \geq 24$. The best fitting parameters we get considering lengths from 27 up to 42 sites gives $U_c = -3.03(1)$, where the error takes into account variations against the system sizes included in the fit. Furthermore, a scaling theory for the height of the peak of χ_F does exist^{42,43} and allows us to obtain the correlation length critical exponent via

$$\chi_F(U^*) \sim L^{2/\nu}.\tag{7}$$

Note that this power-law scaling is independent of the value of the dynamical critical exponent z. In this way we get a value of ν in perfect agreement with the expected value for the Potts model universality class, see Fig. 2(c).

Finally, we wish to mention a very peculiar fact which allows to locate the critical point with arbitrary precision and arbitrary small system sizes: exactly at the critical point, the on-site boson density has vanishing finite-size corrections. The position of U_c can thus be obtained by measuring the boson density for different system sizes and tuning the couplings until size-independence is observed. We believe that this fact is due to the integrable structure beyond the critical spin chain. In Fig. 3, we report the finite-size scaling of the density at the critical point and for two values of U very close to it, together

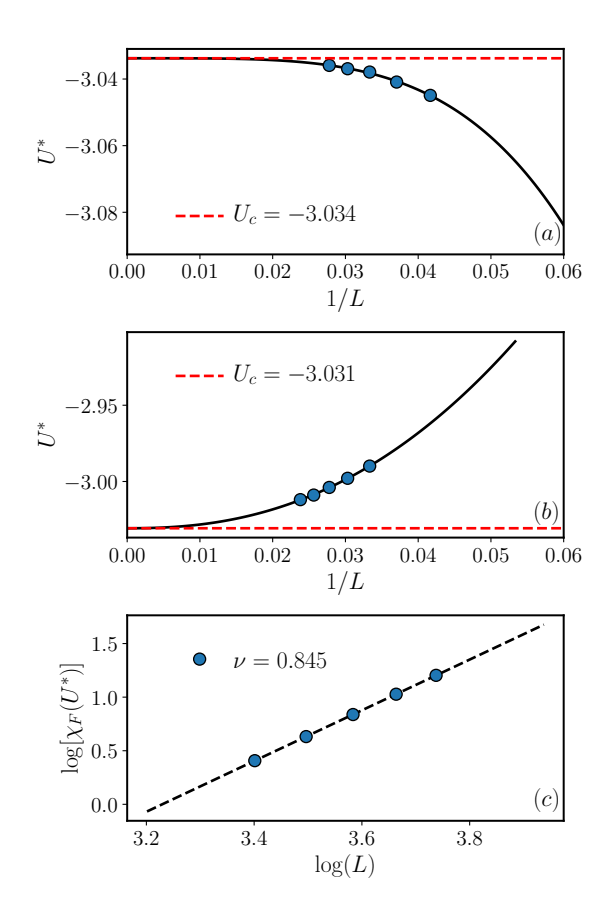


Figure 2. (a) Power-law fit of the peak position $U^*(L)$ of the first derivative of the concurrence Eq. (5), for L from 24 to 36 sites. The scaling exponent extracted from this range of system sizes is $\gamma = 4.0 \pm 0.1$, but it is not stable including smaller sizes. The critical position we get from the fit is $U_c = -3.03 \pm 0.04$. (b) Power-law fit of the peak position $U^*(L)$ in the fidelity susceptibility Eq. (6), for L from 30 to 42 sites. The result is stable when smaller system sizes are included. Keeping into account small variations w.r.t. the range of lengths employed in the fit, the scaling exponent and the critical point position we get are $\gamma = 2.4 \pm 0.1$ and $U_c = -3.03 \pm 0.01$. (c) Scaling of the maximum of χ_F according to Eq. (7) for L from 30 to 42 sites. The correlation length critical exponent slightly increases when smaller system sizes are included in the fit. By taking into account variations w.r.t. the range of lengths fitted we get $\nu = 0.84 \pm 0.01$, in good agreement with the exact value $\nu = 5/6 = 0.8333...$

with the curve crossing of densities computed for different system sizes as a function of U for $V = V_c$, which allows a precise determination of the position of the critical U.

B. Entanglement entropy

Continuous, relativistic phase transitions in 1D system display a logarithmic divergence of the entanglement entropy. Once conformal invariance is ensured, an inexpensive way to identify the universality class is by com-

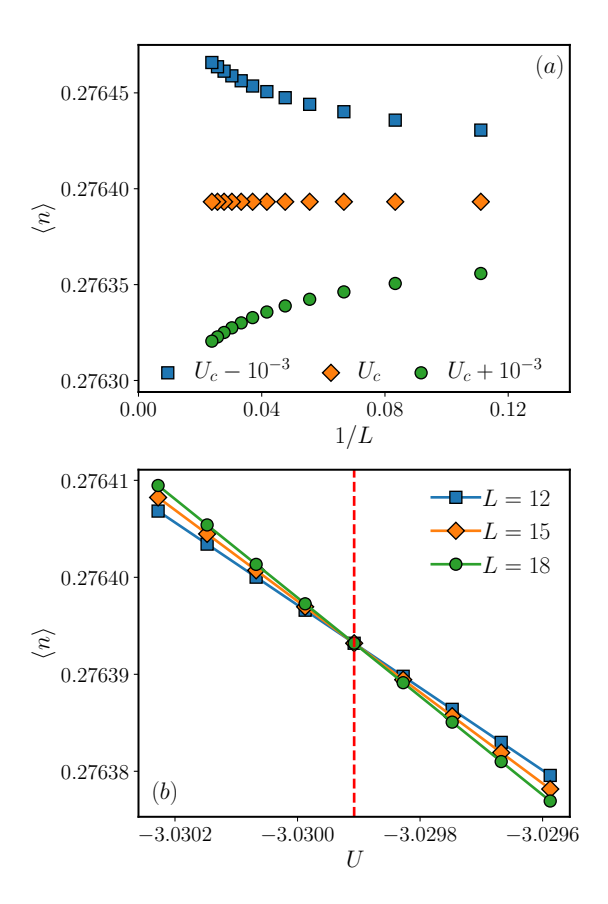


Figure 3. (a) Finite-size scaling of the boson density at the transition point and close to it. Exactly at the transition point, the density does not scale. (b) Boson density as a function of U for $V=V_c$ and different chain lengths. The lines sharply cross at the transition point (dashed red line) for any system size, since finite-size corrections vanish exactly at the critical point.

puting the coefficient of the logarithmic growth of the entanglement as a function of the subsystem size. This coefficient is known to be proportional to the central charge of the ${\rm CFT^{44}}$, and for the case of half-partition in PBC reads

$$S = \frac{c}{3}\log L + A. \tag{8}$$

In Fig. 4(a), we plot the entanglement entropy for the critical values (U_c, V_c) analytically known. This result shows how moderate sizes are already yielding a very precise value for the central charge. In Fig. 4(b), the effective central charge, defined as⁴⁷:

$$c = 3 \frac{S(2L) - S(L)}{\log 2},$$
 (9)

is plotted for fixed $V = V_c$, and varying U across the transition. The central charge exhibits a bell-shape dependence on U, observed in other cases as well⁴⁸, with a peak which is approaching the expected position marked

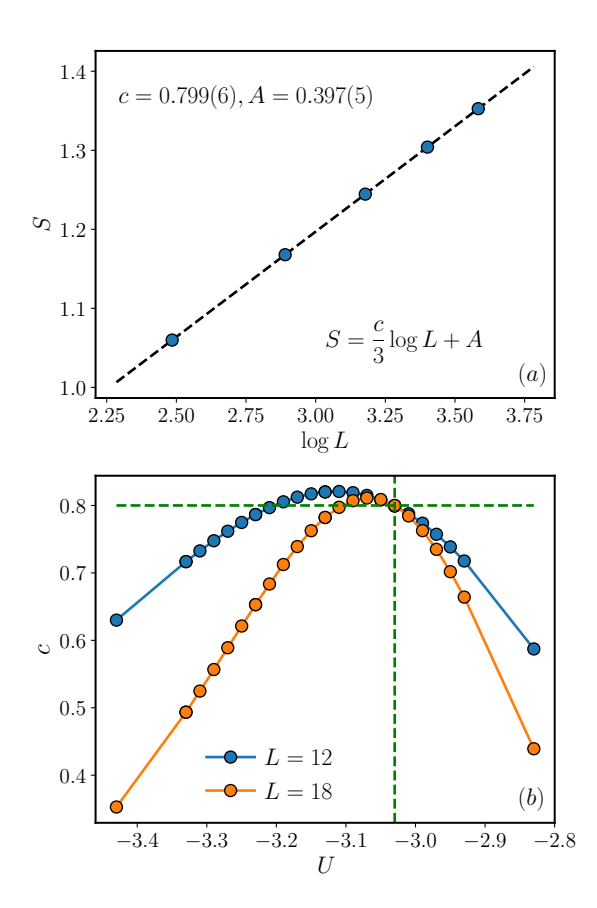


Figure 4. (a) Finite-size scaling of the entanglement entropy of a half-partition, for L from 12 to 36 sites. The slope is the one expected from CFT already for system sizes $L \leq 24$, indicating negligible finite-size corrections to the CFT predictions Eq. (8).(b) Effective central charge as defined in Eq. (9). The peak is sharpening as the system size is increased and the peak position is moving towards the expected value $U_c = 3.0299...$ Curves for different lengths cross almost exactly at this value of U, indicating the presence of a single critical point in which the effective central charge is non-decreasing.

with a green dashed line. Note that different bells touch only at the critical point, which is the only value of U at which the effective central charge is not decreasing with increasing system size. This is in agreement with Zamolodchikov's theorem⁴⁹ in the presence of a single critical point.

C. CFT level spectroscopy

Computing the entanglement entropy is a convenient way of extracting universal information from a quantum spin chain, since it does not involve non-universal parameters like the sound velocity. However, the central charge alone does not uniquely identify the CFT. The full operator content for a CFT on a ring of length L can be determined from the energy levels, which are spaced

according to the formula²³

$$E_n - E_{GS} = \frac{2\pi v}{L} (\Delta + m + \overline{\Delta} + \ell) \qquad m, \ell \in \mathbb{N} \quad (10)$$

where n is a label for the n-th excited state, $(\Delta, \overline{\Delta})$ are the weights of the two chiral representations of the Virasoro algebra in the CFT, and v is the non-universal sound velocity, which depends on the microscopic realization of the CFT. The ground state energy itself is affected by universal finite-size corrections proportional to the central charge

$$E_{GS} = \varepsilon_0 L - \frac{\pi vc}{6L},\tag{11}$$

where ε_0 is the ground state energy density in the thermodynamic limit. Below, we analyze the spectrum obtained by exact diagonalization of the lattice Hamiltonian, for systems with L < 42, in each momentum sector⁵⁰. After extracting the central charge from the entropy scaling, Eq. (11) allows us to compute the sound velocity. The result we obtain by fitting the ground state energy for L up to 42 is v = 2.49(7). Another possibility is to fit directly the dispersion relation of the low energy states, which should be linear and proportional to v. A sample of the low-lying spectrum is shown in Fig. 5(a) for a system of L=39. To obtain the velocity, we perform a linear fit of the smallest available momentum at each system size. The value of v obtained in this way is different for right and left moving particles, and in both cases deviates from the velocity extracted from the ground state energy by a few percents (see Fig. 5(b)). This is caused by large finite-size corrections affecting these eigenvalues. This chiral symmetry breaking at finite-size might be caused by the chiral perturbation driving the system on the second order transition line. Interestingly, by taking the average of the corresponding right and left energy levels, the dominant terms of these corrections cancel out, and full agreement with the value extracted from the GS energy scaling is recovered.

Once the sound velocity is known, Eq. (10) can be used to extract all the conformal dimensions from the gaps in the low energy spectrum of the lattice Hamiltonian. The operators in the CFT are labeled by a \mathbb{Z}_3 quantum number⁵¹ $Q = 0, \pm 1^{34,35}$. Since the model does not have an exact \mathbb{Z}_3 symmetry, we have to find an alternative way of labeling the low-lying states.

The $Q=\pm 1$ sectors have to be degenerate and this degeneracy is exact at finite size in the spectrum of the lattice Hamiltonian Eq. (1) with PBC. This fact is ensured by the presence of the non-commuting momentum and reflection symmetries, which implies that eigenstates of H with momentum K and -K have the same energy. In the \mathbb{Z}_3 -ordered phase and close to it the states with momentum $K=\pm 2\pi/3$ happen to be the lowest energy excitations above the ground state and the Brillouin zone appears to be split in three, as shown in Fig. 5(a). It is thus clear how to identify the \mathbb{Z}_3 symmetry sectors: the neutral sector and the two charged sectors consist of the

energy levels close to K=0 and $K=\pm 2\pi/3$ respectively. This labeling naturally connects to the symmetry-breaking structure of the ground state manifold within the ordered phase.

The operator content of the two non-degenerate symmetry sectors in the CFT with PBC is³⁴:

$$Q = 0: \quad (0,0), \left(\frac{2}{5}, \frac{2}{5}\right), \left(\frac{7}{5}, \frac{2}{5}\right), \left(\frac{2}{5}, \frac{7}{5}\right),$$
$$\left(\frac{7}{5}, \frac{7}{5}\right), (0,3), (3,0), (3,3) \quad (12)$$

$$Q = \pm 1:$$
 $\left(\frac{1}{15}, \frac{1}{15}\right), \left(\frac{2}{3}, \frac{2}{3}\right).$ (13)

The eigenvalues of the lattice Hamiltonian are then spaced according to Eq. (10) and they correspond to the CFT operators above, with all their descendants $(\Delta, \overline{\Delta})_{(k,\ell)}$. However, not all the descendants are allowed and their degeneracy can be computed starting from the Rocha-Caridi formula³⁵. The momentum of these states in the CFT is instead given by

$$\tilde{P} = \frac{2\pi}{L}P = \frac{2\pi}{L}(\Delta + m - \overline{\Delta} - \ell) \qquad m, \ell \in \mathbb{N}. \quad (14)$$

Note that the CFT momentum is not the lattice momentum for this Hamiltonian. The CFT momentum on the lattice is measured starting from the ground states of each \mathbb{Z}_3 sector, which we label by P = 0 (see Fig. 5(a)).

We now proceed with the matching of the low-energy gaps on the lattice with the CFT prediction Eq. (10). Following Ref. 35, we define the universal function

$$\mathcal{F}(Q,P) = \frac{L}{2\pi v} \left(E_P^Q - E_{GS} \right) \underset{L \to \infty}{\sim} \Delta + k + \overline{\Delta} + \ell, (15)$$

where Q and P are the CFT \mathbb{Z}_3 quantum number and momentum.

The results of the field correspondence are presented in Fig. 6. Upon taking proper combinations of degenerate gaps, the finite-size corrections are of order L^{-2} for all the gaps, with a prefactor smaller than 10^{-3} for the lowest ones. We extrapolate the value of $\mathcal F$ by a two-parameter fit for system sizes up to L=42. The agreement of the extrapolation with the CFT expected values is perfect once the sound velocity is tuned to v=2.49225. In this respect, this method is the best way to estimate the sound velocity with the available system sizes.

The finite-size corrections to the universal function in Eq. (15) have been studied for this universality class in the 3-states Potts chain³⁴. It was observed that their power-law exponent was 2 for most of the non-degenerate gaps and a number between 0.5 and 1 for other degenerate gaps. Here we argue that the latter corrections appear only in CFT states $(\Delta, \overline{\Delta})_{(k,\ell)}$ for which $(\Delta, k) \neq (\overline{\Delta}, \ell)$. Upon taking the average of the eigenvalues in which Δ, k and $\overline{\Delta}, \ell$ are exchanged these dominant

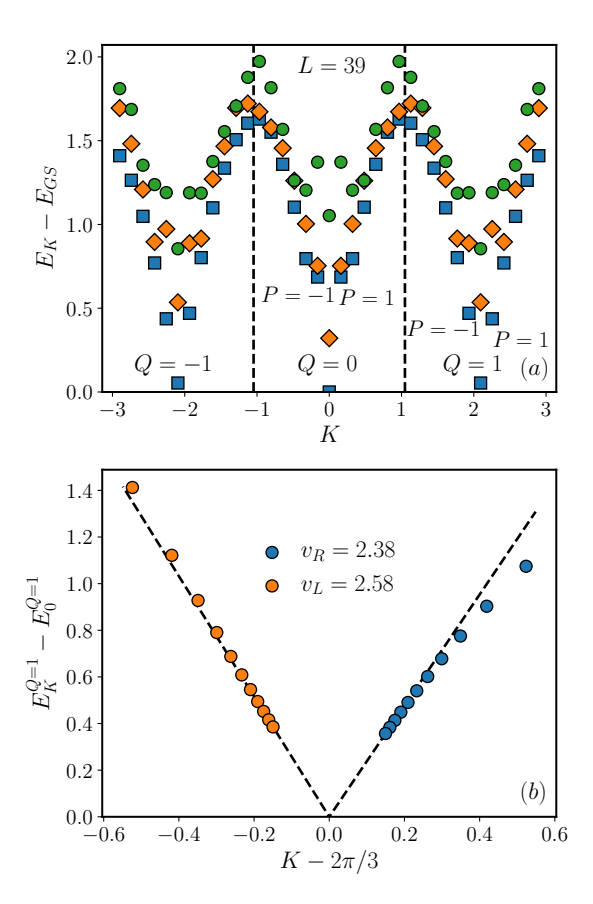


Figure 5. (a) Lowest lying eigenvalues of each lattice momentum sectors for a chain of length L=39. Eigenvalues close to K=0 and $K=\pm 2\pi/3$ correspond to the \mathbb{Z}_3 sectors Q=0 and $Q=\pm 1$ in the CFT. Conformal towers are already distinguishable and primary operators corresponding to each energy level can be easily guessed by comparing the lowest gaps with Eq. (14) together with Eqs. (12), (13). (b) Linear fitting of the lowest eigenvalue close to the ground state of the Q=1 sector for different system sizes from L=12 to L=42. The zero reference energy is taken as the ground state energy of the sector for the given system size. Chiral symmetry is broken on the lattice, most likely because of an irrelevant perturbation which scales away in the thermodynamic limit.

corrections vanish. Formally

$$\mathcal{F}(\Delta, \overline{\Delta}, k, \ell) = \Delta + \overline{\Delta} + k + \ell + \frac{A_{k,\ell}^{(\Delta, \overline{\Delta})}}{L^{\gamma}} + \frac{B_{k,\ell}^{(\Delta, \overline{\Delta})}}{L^{2}} + \dots$$
$$A_{k,\ell}^{(\Delta, \overline{\Delta})} = -A_{\ell,k}^{(\overline{\Delta}, \Delta)}$$
(16)

To support this statement we give two examples where this is manifest. We take the lowest lying pair of states in the Q=1 sector of H with momentum $P=\pm 1$, i.e. $(1/15,1/15)_{(1,0)}$ and $(1/15,1/15)_{(0,1)}$. We then take the pair of states in the Q=0 sector with momentum P=0, i.e. $(2/5,7/5)_{(1,0)}$ and $(7/5,2/5)_{(1,0)}$. On the spin chain these two states correspond to the second and fifth excited state in K=0 sector. Their finite-size scaling is

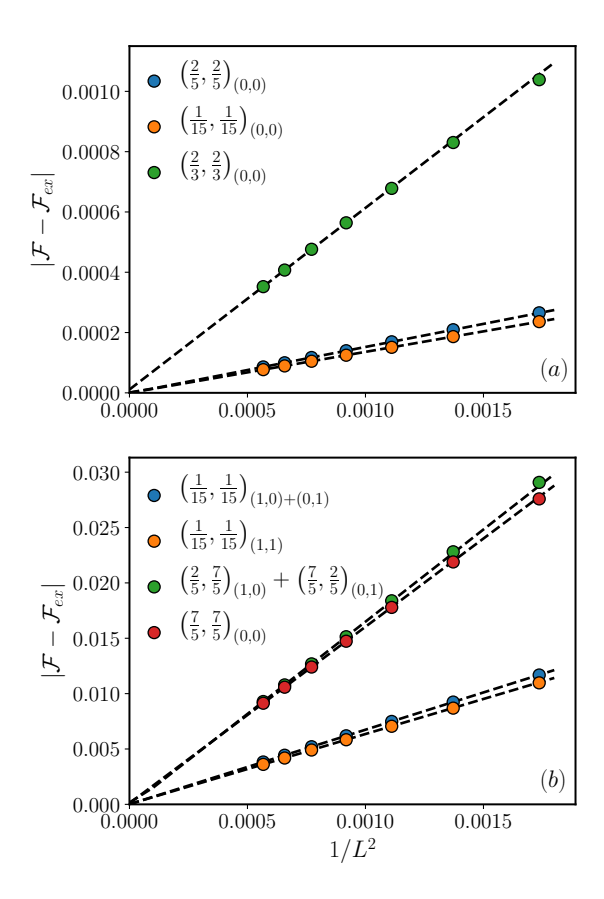


Figure 6. Finite-size scaling of the universal function \mathcal{F} in Eq. (15) w.r.t. the CFT expected value. (a) First and second gaps in the Q=1 sector (orange and green) and first gap in the Q=0 sector (blue). Finite-size corrections scale as L^{-2} with a coefficient of magnitude 10^{-4} for the first two gaps. (b) Third gap in Q=1 sector (orange), first gap in the Q=1 sector with momentum $P=\pm 1$ (blue), average of the second of fifth gap (green) and third gap (red) in the Q=0 sector. The finite-size corrections are always quadratic in the inverse length of the chain upon appropriate average between CFT states not invariant under $(\Delta, k) \leftrightarrow (\overline{\Delta}, \ell)$.

plotted in Fig. 6(b), where these two gaps are denoted by blue and green circles, respectively. The same agreement is observed with many other levels not reported here. We are able to match irrelevant CFT operators with large conformal weights as (0,3), (3,0) and (3,3) and the rule for which the dominant finite-size corrections cancel still applies.

D. Density and order parameter two-point functions

It is, in general, a difficult task to associate matrices on the lattice to primary fields in the CFT. The operator for which this procedure is trivial is the order parameter, namely the most relevant operator in the CFT which is not invariant under a symmetry transformation, i.e. the primary field (1/15, 1/15). Its anomalous dimension is thus $\eta_{\sigma} = 4/15$ and its two-point function is expected to behave as a power-law with this exponent. \mathbb{Z}_3 order is realized on the lattice through a period-3 boson-density wave, thus the (complex) order parameter takes the form¹⁷

$$O_i = n_i + e^{i2\pi/3} n_{i+1} + e^{-i2\pi/3} n_{i+2}.$$
 (17)

Exploiting translational invariance, we can write its twopoint function in terms of the density two-point function as

$$\langle O_r^{\dagger} O_0 \rangle = 3 \langle n_0 n_r \rangle + e^{i2\pi/3} \left(2 \langle n_0 n_{r+1} \rangle + \langle n_0 n_{r-2} \rangle \right) +$$

$$+ e^{-i2\pi/3} \left(2 \langle n_0 n_{r-1} \rangle + \langle n_0 n_{r+2} \rangle \right). \tag{18}$$

If translational invariance can be assumed in the system (as in our case), this quantity will be purely real; a very small imaginary part will be obtained when determining $\langle O_r^{\dagger} O_0 \rangle$ from numerical data, and will be neglected. In order to take into account finite-size effects, we compare our results to the two-point function of the order parameter for a CFT on a ring of length L. For a primary field with conformal weights $\Delta = \overline{\Delta} = \eta/4$, this quantity reads²³

$$\langle O(x)O(y)\rangle = \frac{A}{\left[L\sin\left(\frac{\pi(x-y)}{L}\right)\right]^{\eta}} = \frac{A}{L^{\eta}}G\left(\frac{x-y}{L}\right).$$
 (19)

We can then obtain an estimate of η by fitting the lattice two-point function with the expression above and free parameters A and η . In Fig. 7(b) we plot the lattice expectation value for different system sizes, rescaled by multiplication by L^{η} (where the value resulting from the fit mentioned above is taken for the latter), obtaining perfect data collapse on the universal scaling function G(x) in Eq. 19. In Fig. 7(a) we plot the connected density-density expectation value, which also fits perfectly the CFT expression, with the same scaling dimension as the order parameter.

IV. DOUBLY-BLOCKADED REGIME

In this section, we study the phase diagram of the model Hamiltonian in Eq. (1) in the limit $V \to +\infty$. When $U \to -\infty$ the system is \mathbb{Z}_3 -ordered and the order parameter in Eq. (17) is non vanishing. For finite and large negative U, the finite size spectrum of the Hamiltonian behaves as in the usual \mathbb{Z}_3 spontaneously symmetry-broken (SSB) scenario: the ground state is non-degenerate and the first two low-lying excited states are exponentially close to it with a gap $\Delta \propto \exp(-L/\xi)$, where ξ is the correlation length. In the limit $U \to +\infty$ the ground state is the non-degenerate state with no bosons and \mathbb{Z}_3 symmetry is not broken. A transition between these two regimes is expected in the middle.

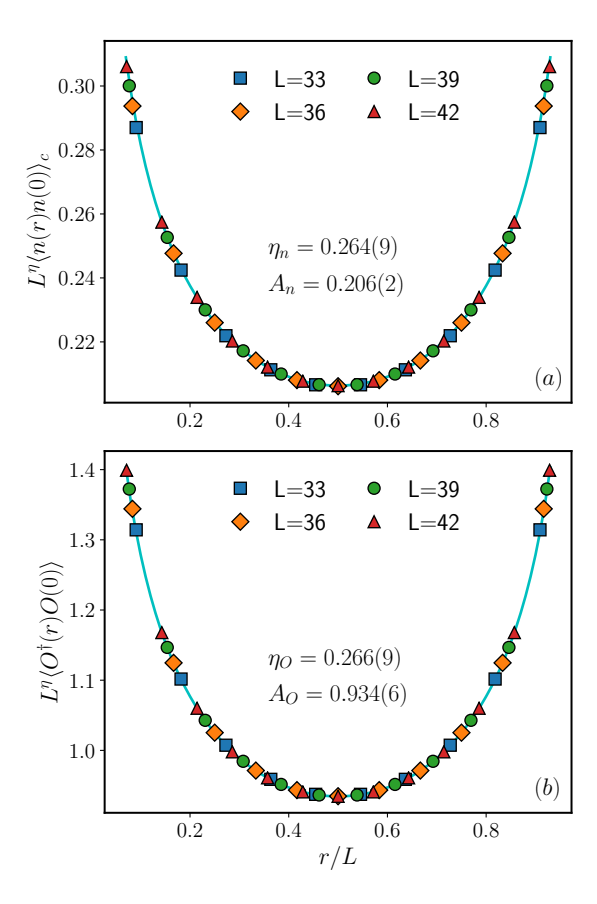


Figure 7. (a) Two-point function of the lattice order parameter Eq. 18 for different lengths L multiplied by L^{η} , with η fitted with the CFT expression Eq. 19. Estimate and error of the amplitude A and the exponent η are obtained upon taking the average of the results for different system sizes. (b) Same scaling as in (a) for the order parameter, which has the same scaling dimension as the density.

In what follows, we provide evidence that there are two continuous phase transitions located at $U_{c1} \lesssim -1.96$ and $U_{c2} \simeq -1.915$. At the first transition, the ground state of the system switches from a period-3 ordered state to a quasi-long-range-ordered, critical phase with incommensurate density-density correlations, known as floating phase. At the second transition point, the system passes from the gapless critical phase to a disordered phase. For the first transition we compute, with different methods, the location of the critical point, the correlation length critical exponent ν , the dynamical critical exponent z and the order parameter critical exponent β . We then show that the second transition is consistent with the BKT scaling ansatz, according to which the correlation length vanishes exponentially and the gap finite-size scaling at the transition point is affected by logarithmic corrections 52 .

We finally show that for values of U inside the floating phase $U_{c1} \leq U \leq U_{c2}$ the scaling of the entanglement entropy is in agreement with the Luttinger liquid univer-

sality class, where the central charge c equals 1.

A. Quantum concurrence and fidelity susceptibility

By means of the same methods tested in Sec. III A, we now proceed to investigate the transition points by studying the behavior of the quantum concurrence and the fidelity susceptibility. These observables are not known to be generically sensitive to BKT transitions⁵³: for this reason, we expect them to only diagnose the presence of the first of the two transitions mentioned above. We carry out exact diagonalization calculations up to L = 54 sites for ground state properties, and consider sizes $L = 3n, n \in \mathbb{N}$ to avoid incommensurability effects.

The derivative of the concurrence exhibits the same behavior discussed in Sec. III A, namely a peak which is sharpening and moving towards the critical point, U_c , with increasing system size. In order to extrapolate the position of the maximum $U^*(L)$ for $L \to \infty$ we fit it with a power-law with scaling exponent $\gamma = 1$. In this way, we obtain a value $U_{c1} = -1.969 \pm 0.005$, which is stable against the range of systems sizes included in the fit. By performing the same analysis for the peak of the fidelity susceptibility, Eq. 6, we get instead a critical value $U_{c1} =$ -1.973 ± 0.005 . The results are plotted in Fig. 8(a)-(b). Both of these results illustrate the fact that finite-size effects in this regime are comparatively larger than close to the Potts critical point. In particular, employing sizes of the order $L \simeq 30$ would lead to wrong estimates in both cases: the scaling regime for what concerns entanglement and wave-function properties seems to be only reached above L = 33.

Exploiting the known finite-size critical scaling of the peak of χ_F described by Eq. 7, we obtain a critical exponent $\nu = 0.70 \pm 0.05$. We stress that the latter estimate is very sensitive to the system sizes employed in the analysis. In particular, the larger the system sizes included in the fit, the smaller the ν obtained (see Fig. 8(c)). In Ref. ¹⁹, the value $\nu \simeq 5/7$ was extracted from data collapse of the gaps, assuming the value $z \simeq 4/3$ for the dynamical critical exponent. This evidence was used to conclude that the transition does not belong to the PT universality class, for which $\nu = 1/2$ and z = 2. Although the variation of the exponent with the system sizes considered seems very slow, we cannot exclude, based on our data, that it eventually reaches the value expected for a phase transition of the PT type, as found in Ref. 20 for the critical regime below the Potts point.

B. Critical point location through data collapse

We now exploit the finite-size scaling theory which applies in the proximity of a second order phase transition⁵⁴ to extract the values of U_{c1} , z and ν from the lowest spectral gap Δ . With this aim, we adopt an approach very similar to the one taken in Refs. 55 and 56.

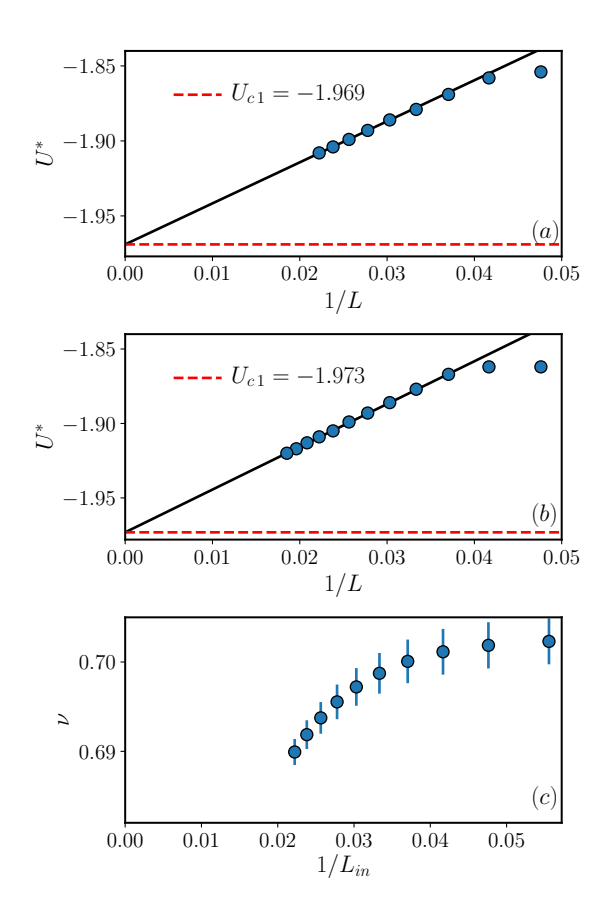


Figure 8. (a) Linear fit of the peak position $U^*(L)$ of the first derivative of the quantum concurrence Eq. (5) vs 1/L, for L from 33 to 45 sites. The result of the fit is stable against the system sizes included in the fit and the critical position we obtain $U_{c1} = -1.969 \pm 0.005$, where the error takes into account variations w.r.t. the system sizes included in the fit. (b) Linear extrapolation of the peak position $U^*(L)$ vs 1/L in the fidelity susceptibility Eq. (6), for L from 39 to 54 sites. The result is stable when smaller system sizes are included and the critical point position we get is $U_{c1} = -1.973 \pm 0.005$. Error considerations are the same as in panel (a). (c) Correlation length critical exponent obtained from the scaling of the maximum of χ_F according to Eq. (7) for $L = L_{in}, L_{in} + 3, ..., 54$ as a function of L_{in} . The critical exponent decreases when smaller system sizes are excluded from the fit and saturation is not reached with the maximum lengths we can access. We note that a strong sensitivity of critical exponents with respect to system sizes was already noted in Ref. 20.

First we compute a universal scaling function F from ED data for Δ for different system sizes. This scaling function will depend on some unknown critical exponent γ and on the dimensionless ratio L/ξ , L being the system size and ξ the correlation length: $F = F(\gamma, L/\xi)$. We then assume a functional form for ξ in terms of the critical point position U_c and, if finite, of its critical exponent ν : $\xi = \xi(U, U_c, \nu)$. We use this functional form to express the scaling function F in term of the variable $x = \log(L/\xi) = x(L, U, U_c, \gamma, \nu)$. Finally, we combine

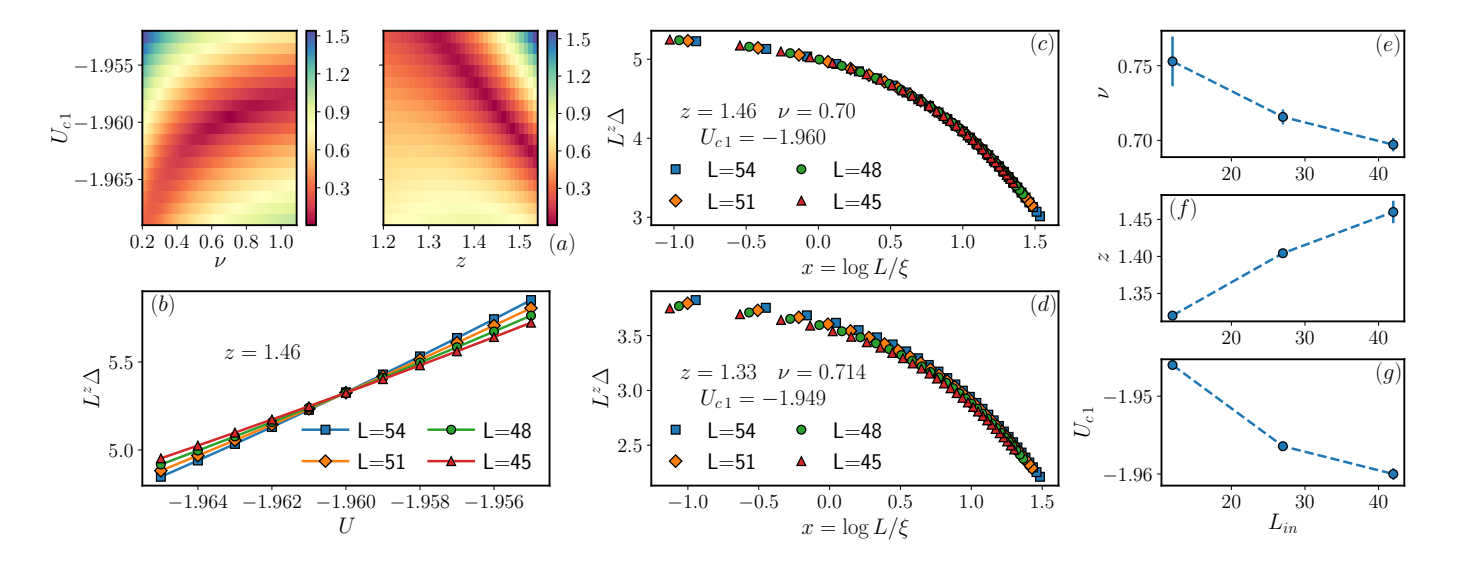


Figure 9. (a) Density plot of the square root of the sum of the squared residuals in the (ν, U_{c1}) and (z, U_{c1}) planes for the best values fitting values of z and ν respectively. (b) Crossing of the gaps, upon multiplication by L^z for the best fitting z. The crossing indicates the position of the critical point. (c) Data collapse of ED numerical data, with $U \in [U_{c1} - 0.03, U_{c1}]$ with the parameters U_{c1}, z, ν which minimize the polynomial fit of the universal scaling function in Eq. (20). (d) Same as in (c), but with parameters U_{c1}, z, ν taken from Ref.19. (e)-(f) Critical exponents and critical point location obtained by applying the procedure described in Sec. IV B for sets of 5 system sizes $L = L_{in}, ..., L_{in} + 12$ with increasing L_{in} . The average is obtained by varying the size of the interval $[U_{c1} - \delta U, U_{c1}]$ with $0.01 \le \delta U \le 0.03$, the degree of the polynomial being fixed to 10. The errorbar is the standard deviation of the obtained results.

data for F for different system sizes and we look for the value of U_c, ν, γ which produce the best data collapse. This is achieved by fitting $f(x) = F(e^x)$ with an arbitrary high-degree polynomial and minimizing the sum of the squared residuals. By considering a full functional collapse instead of extracting the thermodynamic limit gap from single parameter data, this method copes relatively well with finite-size effects – even in the most critical BKT scenario. Indeed, in the latter case it allows to locate transition points with a precision similar (if not better) to approaches based on matching conformal dimensions 55,56, which are based on assuming a specific functional dependence between lattice and field theory operators.

Since at a quantum phase transition all low-lying eigenvalues of the Hamiltonian are expected to be separated from the ground state by a power-law decaying gap $\Delta \sim 1/L^z$, where z is the dynamical critical exponent, we can obtain a scaling function by multiplying the lowest gap by L^z

$$F\left(\frac{L}{\xi}\right) = L^z \Delta \,. \tag{20}$$

Assuming that the phase transition has finite ν exponent, we have

$$\xi \sim (U_{c1} - U)^{-\nu}$$
 (21)

We can then find the best fitting values of ν,z and U_{c1} via the procedure described above. It is fundamental to

check the stability of the result w.r.t. the degree of the polynomial, the size of the interval from which the value of $U < U_{c1}$ are taken and, most importantly, the system sizes which are included in the fit. We find that, in our case, the result is very stable w.r.t. the first two, but we get stability w.r.t. the system sizes we have at our disposal only if we include the largest ones (up to $L_{\text{max}} = 54$). In particular, by including sizes of increasing magnitude we observe a decrease in our estimates for U_{c1} and ν , and an increase in the one of z. In Fig. 9(c) we show the result obtained by including all systems sizes $45 \le L \le 54$. The data collapse shows deviations of order 10^{-2} , and is considerably more accurate than the one performed with the values reported with $L_{\text{max}} = 36$ (see Fig. 9(d)).

However, as shown in Fig. 9(e)-(f), the z and ν exponents are still varying with the system size. Although the trend exhibited by this data does not allow any extrapolation, we clearly see that the true scaling regime has not yet been reached. This leaves open the possibility that z and ν will eventually approach the values expected from a Pokrovsky-Talapov transition, namely 2 and 1/2 respectively³². The best estimates we can give from our data of critical exponents and critical point position are: $z = 1.48 \pm 0.1$, $\nu = 0.7 \pm 0.1$, $U_{c1} = -1.960 \pm 0.005$.

Since the methods employed over the next subsection will rely on assumptions, we find it useful to summarize the analysis performed so far. All diagnostics are compatible with the presence of a second order phase transition. The location and nature of the transition are extremely sensitive to the system sizes investigated. Regarding the location of the transition point, sizes up to $L \simeq 30$ are not sufficient to determine it, while the estimate using all three methods are rather stable after $L \simeq 45$. Entanglement-based methods return $U_{c1} = -1.973 \pm 0.005$ and $U_{c1} = -1.969 \pm 0.005$, respectively. The method based on gap collapse returns $U_{c1} = -1.960$: for this last method, it is challenging to include a rigorous error bar. However, it is worth noting that the best data collapse obtained up to L = 36 returns $U_{c1} = -1.949$, in agreement with Ref. 19: this clearly signals that the critical point is drifting to considerably smaller values of U as size increases (see Fig. 9(g)), in agreement with the entanglement-based diagnostics.

A similar conclusion holds for the critical exponents: as clearly observed in the fidelity susceptibility scaling, even at sizes of order L=54, the critical exponent has not yet reached its thermodynamic value. The data collapse of the finite size gaps fully confirms this picture. This motivates the study in the next subsection, where we will employ different – but assumption-dependent – methods to determine some of the properties of this second order transition. From the analysis performed here, we can anticipate that, even if larger system sizes are studied, depending on the observable, a systematic underestimation of the modulus of the critical point location $|U_{c1}|$ is expected. As we will see, this is particularly critical for the methods discussed in the next section.

C. Order parameter

In this section, we investigate the disappearance of the \mathbb{Z}_3 order across the second order phase transition. We do so by utilizing three methods: a QMC and DMRG study in PBC, and a 1-site DMRG study with OBC. Our focus in the following will be on correlation functions and the order parameter of the \mathbb{Z}_3 order. As such, we will be assuming that there is an exact mapping between the lattice operators describing the latter, and its field theory counterpart. While this condition is typically satisfyingly fulfilled for most lattice models displaying quantum critical behaviour, we opted for a more conservative approach in the context of the FSS in the doubly blockaded regime. The reason is that the constraint acts at the lattice spacing level irrespectively to how close one is to the critical point. This suggests that defining field operators that do not change at the lattice spacing level is non-trivial, making the connection between lattice and continuum not immediate. While this feature has no consequence on spectral and wave-function properties, it is highly likely that it affects the finite-size behaviour of correlation functions.

We perform quantum Monte Carlo (QMC) simulations using a modified version of the Worm algorithm²⁷, adapted to simulate Hamiltonians with off-diagonal terms such as those of the FSS model and with updates designed to automatically respect its occupation con-

straints. The method allows to directly measure quantities such as energy, particle density, and the static structure factor:

$$S(k) \equiv \frac{1}{L^2} \sum_{i,j=1}^{L} e^{-ikr_{ij}} \langle n_i n_j \rangle, \qquad (22)$$

where k is one of the allowed lattice momenta, and r_{ij} is the distance between sites i and j. In the \mathbb{Z}_3 -ordered phase the structure factor will feature a peak at a wavevector $k=2\pi/3$, corresponding to the periodicity of the \mathbb{Z}_3 -periodic charge density waves. The value of the peak is equal to the squared \mathbb{Z}_3 order parameter in Eq. (17), and therefore follows a power-law behavior $S(2\pi/3) \sim |U-U_c|^{2\beta}$ when approaching the critical point U_c from the ordered phase.

We obtained an estimation of the position of the critical point, as well as the critical exponent β , by interpolating the QMC results with the expected power-law behavior. We studied system sizes up to L=120 sites and temperatures down to T = 1/128 (where the magnitude of the off-diagonal part of the Hamiltonian is taken as a unit of energy). Extrapolation in the inverse temperature has been employed to determine ground-state results where direct convergence in T (i.e., results identical within their uncertainty for one or more pairs of temperatures (T, T/2) was not observed. Below U = -1.96, no further extrapolation in the system size was necessary, since direct convergence in size was always observed. Above this value, however, our extrapolated values were not fully converged in size and inverse temperature (also due to considerably slower MC dynamics). We therefore restricted our investigation to the U < -1.96 region. Fig. 10 shows the QMC data (triangles) as well as the power-law interpolation (purple line). The resulting values are $U_{c1} = -1.951(5)$, $\beta = 0.059(7)^{58}$.

An independent estimate of the critical point and critical exponent β has been obtained by computing $S(2\pi/3)$ via DMRG (circles in Fig. 10) and performing the same extrapolation as above (solid green line in Fig. 10). We approximated the exact Hilbert space in the DMRG by giving a large penalty to not-allowed states. This is achieved by adding to the Hamiltonian a term $\lambda \sum_{i} n_{i} n_{i+1} + n_{i} n_{i+2}$, with $\lambda = 10^{3}$. Unfortunately, performing a rigorous extrapolation in $\lambda \to \infty$ is extremely difficult: the main reason is that, for increasingly larger values of λ , the diagonalization at each DMRG step becomes extremely sensitive to numerical errors due to the large difference in the matrix elements of the Hamiltonian matrix. However, for a fixed value of λ , we expect a difference of the order of $1/\lambda$ when comparing local observables, such as energies, with ED data. The absence of any other unforeseen source of systematic error due to the finite value of λ can be confirmed by direct verification. Indeed, with our choice of $\lambda = 10^3$, if we calculate the energy gap between the ground state and the first excited level for L = 54 and U = -1.950, the discrepancy between DMRG and ED is of the (expected)

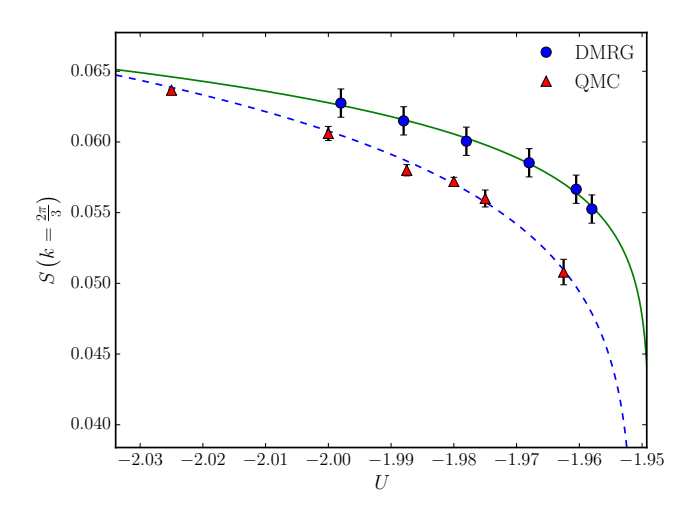


Figure 10. $S(2\pi/3)$ as a function of the parameter U. Symbols represent QMC (triangles) and DMRG (circles) for the ground state of model Eq. (1), extrapolated in the thermodynamic limit (see text). The dashed and solid line are a power-law fitting function (see text) used to interpolate QMC and DMRG results, respectively.

order of $\epsilon_{\Delta} \approx 10^{-3}$. This check is very important because it allows us to understand that the limit $\lambda \to \infty$ is approached perturbatively. Despite this violation of the constraint which directly affects local observables, we obtain a good agreement with ED when we study other quantities such as entanglement entropy and central charge. For instance, using the same values of L and U, we obtain a difference in the central charge of the order of $\epsilon_c \approx 10^{-4}$ with respect to ED results. In our DMRG implementation, we take an elementary cell made of 3 sites in order to have a local representation of the \mathbb{Z}_3 order. This also allows us to discard 4 of the 8 states in the blocked DMRG-site. Simulations were performed by keeping the truncation error below 10^{-7} using up to 1000 DMRG-states and ensuring that the energy variance of the ground-state is of the same order of the truncation error.

We observe that DMRG results (after an extrapolation in 1/L of the squared \mathbb{Z}_3 order parameter for $84 \leq L \leq 120$) yields a larger value for $S(2\pi/3)$ than QMC, possibly due to the approximations required to impose the occupation constraint. The results of the extrapolation are $U_{c1} = -1.948 \pm 0.007$ and $\beta = 0.036 \pm 0.005$.

As a final test-bed for the results above, we compute directly the order parameter in Eq. (17) by variationally optimizing the ground state with MPS methods on an open chain in which the constraint is implemented exactly. The method we use exploits the exact relation between MPOs and finite state automata⁵⁹, and is described in detail in the Appendix. We are able to variationally optimize the MPS for chains of up to 718 sites. The computational resources required to accurately approximate the ground state are relatively small: a bond dimension of 200-300 is sufficient to keep the variance

of the Hamiltonian below 10^{-9} . We explicitly break \mathbb{Z}_3 symmetry by choosing system sizes which are multiple of 3 plus 1 site. This makes energetically favored states in which there are two bosons at the edges, thus breaking the symmetry without adding any term in the Hamiltonian. Extrapolation to the thermodynamic limit is then performed vs 1/L. The result is plotted in Fig. 11. We compute the order parameter by averaging the one-point function on L/2 sites in the bulk. The fit of the averaged order parameter as a function of U returns a critical exponent $\beta = 0.031 \pm 0.005$ and a critical point location $U_{c1} = -1.969 \pm 0.002$. The error attributed takes into account variations of the fitting parameters obtained by considering different sets of values of U and computing the order parameter by performing the average over a different number of sites in the bulk of the chain.

Summarizing, the direct study of the order parameter provides similar information to that of the quantities analyzed in the previous subsection: upon increasing system sizes, the position of the second order transition systematically drifts toward larger values of $|U_{c1}|$. It is informative to note that this shift is compatible with a 'finitesize' location of the transition point based on the wavefunction variation captured by the fidelity susceptibility: as it can be seen from Fig. 8(b), a finite-size estimate at around $L \simeq 120/800$ would return a critical coupling of order $U_{c1} \simeq -1.95/1.97$, respectively. The incompatibility with the extrapolated values of the structure factor between DMRG and QMC indicates that approaching an exactly blockaded regime in experiments is challenging (see, e.g., the relatively large deviations in estimating β), even if, in terms of transition point location, the difference is of order 0.003.

D. BKT transition and the floating phase

The presence of a systematic drift towards smaller values of U_{c1} as a function of the system size may signal the presence of an intermediate phase between the ordered and disordered ones. A first check on this hypothesis can be obtained via investigation of the entanglement entropy. To this end, we perform DMRG simulations up to L = 108 sites. In Fig. (12) we plot the entanglement entropy for fixed U = -1.95 as a function of the cord distance on the ring $\kappa(\ell) = L/\pi \sin(\ell\pi/L)$, ℓ being the length of the subsystem on the lattice, for different system sizes. By directly fitting the scaling of the entropy for this value of U, which belongs to the region between U_{c1} and U_{c2} according to all our estimates, we are able to obtain a central charge in a good agreement with a c=1CFT. This is a strong indication of the presence of a critical phase for $U > U_{c1}$, compatible with the Luttinger liquid universality class. We note that, for non-relativistic critical points or phases, the entanglement entropy is not bound by a logarithmic growth, and even if so, the coefficient could be arbitrary. This implies that, assuming there is no fine-tuning, a c=1 point or phase is present

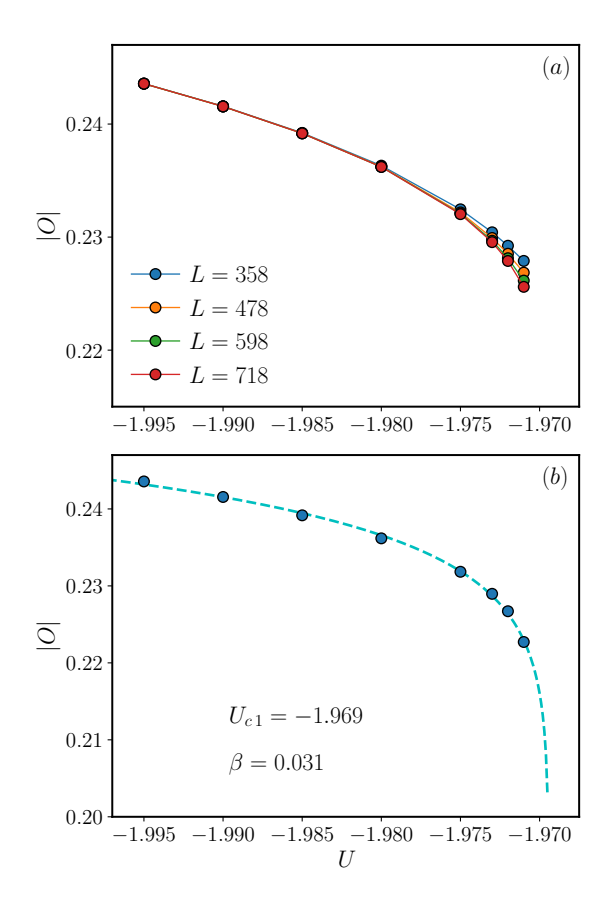


Figure 11. (a) Order parameter computed by averaging the one-point function $O_j = e^{i2\pi j/3} n_j$ on L/2 sites in the bulk. \mathbb{Z}_3 symmetry is spontaneously broken by the choice of the number of sites on the open chain, i.e. a multiple of 3 plus 1 site. The obtained order parameter does not scale with the system size for U < -1.975. (b) Infinite-size limit value of the order parameter, extrapolated in 1/L and power-law fit of the resulting curve. The obtained critical exponent and critical point position are $\beta = 0.031 \pm 0.005$ and $U_{c1} = -1.969 \pm 0.002$.

here.

As discussed above, all entanglement-related quantities signal a single second order phase transition. This implies that the transition between the IC and disordered phase shall belong to the BKT universality class, in agreement with field theoretical insights^{17,20}.

By carrying out the same analysis of section IVB on the lowest gap in the energy spectrum, we can estimate the location of the BKT transition, which is expected to occur for $U \geq -1.95$. The scaling ansatz differs from the one in the previous section for two reasons: the dynamical critical exponent is z=1, and the exponential divergence of the correlation length is:

$$\xi \sim \exp\left(\frac{b}{\sqrt{U - U_{c^2}}}\right),$$
 (23)

where b is a non-universal constant, independent of U. Moreover, logarithmic corrections are known to intervene

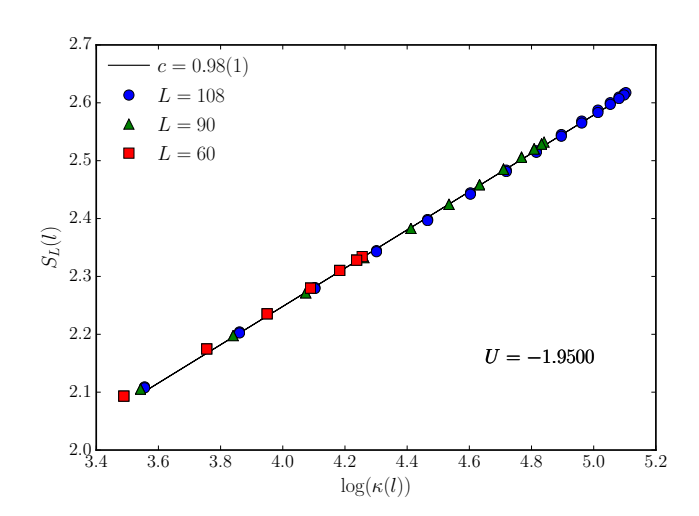


Figure 12. Entanglement entropy for fixed U inside the floating phase as a function of the logarithm of the cord length in the CFT ring. The fit produces a central charge in a perfect agreement with the Luttinger liquid CFT.

at the end of RG lines of fixed points. In the case of a BKT point the functional form of these corrections is known to be⁵² $\Delta \sim L^{-1}[1+1/(2\log L+C)]^{-1}$, for some model-dependent constant C. On the basis of this field theory result we take as scaling function for the gap^{55,56}

$$\Delta^* = L\left(1 + \frac{1}{2\log L + C}\right)\Delta = F\left(\frac{L}{\xi}\right). \tag{24}$$

This scaling ansatz, in combination with the procedure previously discussed, has been tested in various spin chains where the location of the BKT transition point was analytically known⁵⁶. In these cases, the method was found to slightly underestimate the width of the gapless region: in our case here, one thus expects that this method will overestimate the value of $|U_{c2}|$. In terms of accuracy, the estimate obtained with this method is compatible with state-of-the-art diagnostics based on targeting operator dimensions via correlation functions.

In our case, we observe the same shifting of the critical point towards negative U as we take increasingly large system sizes. A sample result of the largest system sizes we have investigated is plotted in Fig. 13: the quality of the data collapse is excellent, as testified by the small value of the sum of the discarded weights. By taking into account variations of the optimal parameters w.r.t. the set of system sizes and amplitude of the intervals considered, we get $b=0.27\pm0.05, C=10.0\pm0.5, U_{c2}=-1.915\pm0.008$ as the best estimate of the scaling function and transition point location.

V. CONCLUSIONS

In this work, we have investigated the physics of the hard-core boson constrained model of Eq. (1) in the re-

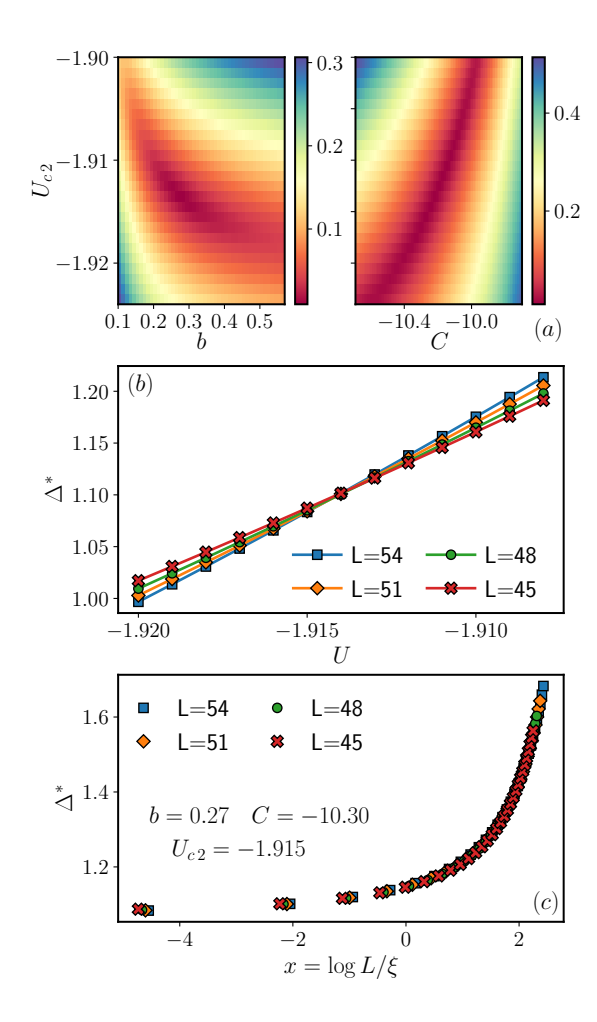


Figure 13. (a) Density plot of the square root of the sum of the squared residuals in the (b, U_{c1}) and (C, U_{c1}) planes for the best-fitting values of C and b respectively. (b) Crossing of the logarithmically-corrected gaps, upon multiplication by L^z (where z=1) and taking the best-fit value for C. The crossing indicates the position of the critical point. (c) Data collapse of ED numerical data, with $U \in [U_{c2}, U_{c2} + 0.03]$ with the parameters U_{c2}, b, C which correspond to the best polynomial fit of the universal scaling function in Eq. (24).

gion of the phase diagram surrounding the \mathbb{Z}_3 -ordered phase. In the first part of the study, we considered the vicinity of the Potts critical point. Since the position of the latter is analytically known, we have used this regime to benchmark entanglement-based techniques to detect quantum criticality in constrained models. In particular, we have shown how concurrence and fidelity susceptibility are able to accurately determine the exact location of the critical point with accuracy of order 0.1% in units of the coupling U. At the critical point, we have carried out an extensive investigation of the low-lying energy spectrum, matching such spectrum with the one expected from the \mathcal{M}_3 minimal model. Our data suggest that it is possible, within experimentally achievable system sizes, to unambiguously diagnose Potts quantum critic-

ality by just measuring spectral properties. We have also observed systematic suppression of finite-size corrections in local observables, a feature which we believe is due to integrability at the critical point.

In the second part of the work, we have investigated the melting of the ordered phase in the so called 'double-blockaded' regime, that is, in presence of infinite next-to-nearest-neighbor repulsion. We have observed the presence of a gapless regime, i.e., an incommensurate phase, already found in the same model below the Potts transition point. Our results show how this phase is surrounded by a second-order phase transition from one side, and a Berezinski-Kosterlitz-Thouless transition on the other. The position of the latter has been determined using an advanced gap scaling technique at $U_{c2} = -1.915 \pm 0.008$.

Regarding the second order phase transition, we have found that reaching a scaling regime for entanglement (concurrence and fidelity susceptibility) properties requires sizes L > 30. Reaching this regime is also required to determine the location of the transition point utilizing spectral properties. Due to the difficulty in performing calculations for these sizes, entanglement and spectral methods only allow us to provide a lower bound to the position of this critical point, $U_{c1} \lesssim -1.96$. Similarly, we can only provide bounds for the critical exponents: in particular, we find a systematic drift of the value of ν toward smaller values, and of z toward higher values. These findings are not compatible with previous results¹⁹ based on sizes up to L=36, while they are compatible with a potential emergence of Pokrovsky-Talapov critical behavior observed below the Potts point²⁰ and with a series of different non-relativistic critical scenarios proposed in related field theories²¹. Following the analogy between the FSS and the chiral clock model suggested in Ref. 19, our findings indicate that, in the FSS model, the critical line separating the ordered and disordered regimes ultimately reaches the regime corresponding to large chiral angles in the clock model, where an incommensurate phase intervenes between the two phases⁶⁰.

We have complemented our analysis with numerical simulations monitoring the behavior of solid order across the transition, using both quantum Monte Carlo and tensor network methods. These methods predict a position of the phase transition that strongly depends on the considered boundary conditions. In all cases, the position of U_{c2} is well distinct from U_{c1} w.r.t. the numerical uncertainty of our results.

Our results suggest that the strong coupling regime is relatively convenient to observe phases with incommensurate order, as the size of the floating phase is considerably larger than at smaller couplings. Moreover, spectral properties should be favoured as probes over correlation functions, which seem to be more sensitive to finite-size effects. In addition, the presence of a relatively extended transient scaling regime in terms of system sizes partly supports the observation made in Ref. 18 regarding Kibble-Zurek scaling: while the combined effects of a second order and nearby BKT transition have

not been discussed in detail to the best of our knowledge, it is likely that the presence of the latter affects rather dramatically the dynamics over parameter space, due to exponentially vanishing gaps. We leave the investigation of such a scenario (which has been shown to be experimentally achievable¹⁵) to a future study. Finally, it would be interesting to systematically consider the effect of additional interaction terms that are present in experiments: despite their modest magnitude (as they decay very similarly to van der Waals interactions), those terms may sensibly affect the size of the incommensurate phase.

Acknowledgements

We acknowledge useful discussions with C. Castelnovo, R. Fazio, P. Fendley, V. Khemani, C. Laumann, F. Mezzacapo, N. Pancotti, H. Pichler, L. Piroli, S. Sachdev, and A. Sterdyniak. This work is supported by the ERC under grant number 758329 (AGEnTh). MDM acknowledges computing resources at Cineca Supercomputing Centre through the Italian SuperComputing Resource Allocation via the ISCRA grant SkMagn.

Appendix: MPS optimization in constrained Hilbert spaces

We summarize our method to simulate constrained one-dimensional systems with tensor network techniques. As opposed to local constraints or symmetries, which can be encoded directly at the level of the individual tensors, here we wish to take into account constraints spanning several neighboring sites. In the context of this type of spin models, a recent approach has been implemented in Ref. 20, by keeping track of the possible transitions between valid states when constructing the environment tensors, for the case of NN blockade. Our method instead aims at being slightly more general, in order to accommodate arbitrary non-local constraints — and, in particular, NNN ones — with a low computational overhead. More specifically, we encode a state in the full many-body Hilbert space, and then construct the projector to the specific subspace we are interested in.

For this paper, we consider the Hilbert space $\mathcal{H}_L = (\mathbb{C}^2)^{\otimes L}$, where we label the local basis by $\{|\circ\rangle, |\bullet\rangle\}$. States in \mathcal{H}_L can be represented by MPS with a local physical dimension d=2. We can then construct the projector \mathcal{P} onto the subspace of interest as an MPO. The construction of an arbitrary operator can be achieved by exploiting the correspondence between MPOs and finite state automata⁵⁹. We label the internal states as 1,2,.... In the case of the single constraint $n_i n_{i+1} = 0$, the only

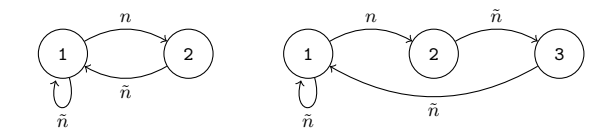


Figure 14. Finite state automaton corresponding to the nearest-neighbor (*left*) and next-nearest-neighbor (*right*) projector. Notice that there is not a clear initial and final state, as in the case of Hamiltonians, but these automata form a cycle.

non-zero entries on each tensor of the projector are

$$1 - \begin{array}{c} \circ \\ -1 \\ \circ \\ -1 \end{array} = 1 - \begin{array}{c} \bullet \\ -1 \\ \circ \\ -1 \end{array} = 2 = 2 - \begin{array}{c} \circ \\ -1 \\ \circ \\ -1 \end{array} = 1 \quad (A.1)$$

which corresponds to the finite state automaton on the left of Fig. 14. The corresponding MPO tensor for the projector is

$$P_{ab} = \begin{pmatrix} \tilde{n} & n \\ \tilde{n} & 0 \end{pmatrix} \tag{A.2}$$

where $\tilde{n} = |\circ\rangle \langle \circ|$ and $n = |\bullet\rangle \langle \bullet|$. Similarly, we can construct the projector with next-nearest-neighbor interaction, i.e. we want to simultaneously impose $n_i n_{i+1} = 0$ and $n_i n_{i+2} = 0$. We modify the previous approach and add the diagrams

$$1 \xrightarrow{\circ} 1 = 1 \xrightarrow{\bullet} 2 = 2 \xrightarrow{\circ} 3 = 3 \xrightarrow{\circ} 1 = 1$$

$$(A.3)$$

This corresponds to the automaton on the right of Fig. 14 and a MPO tensor

$$P_{ab} = \begin{pmatrix} \tilde{n} & n & 0\\ 0 & 0 & \tilde{n}\\ \tilde{n} & 0 & 0 \end{pmatrix} \tag{A.4}$$

To approximate the ground state $|\psi\rangle$ of a certain Hamiltonian H under the constraint, we can then proceed by variationally updating single tensors such that they minimize the projected Hamiltonian $\langle H \rangle =$ $\langle \psi | \mathcal{P} H \mathcal{P} | \psi \rangle$. The optimization algorithm will automatically converge towards a state that satisfies the constraint. This can be understood by decomposing the state into parallel and perpendicular components to the subspace satisfying the constraint: $|\psi\rangle = \alpha |\psi_{\parallel}\rangle + \beta |\psi_{\perp}\rangle$, with the usual normalization $\alpha^2 + \beta^2 = 1$. The energy expectation value is then $\langle \psi | \mathcal{P}H\mathcal{P} | \psi \rangle = \alpha^2 \langle \psi_{\parallel} | H | \psi_{\parallel} \rangle$. Any state in the perpendicular subspace will be an eigenvector of H, with eigenvalue 0. Hence, if the true ground state energy is negative, the optimization algorithm naturally favors the parallel part, sending $\alpha \to 1$, $\beta \to 0$. This condition can always be fulfilled without loss of generality, since

we can always shift the Hamiltonian by a constant to ensure $\langle \psi_{\parallel} | H | \psi_{\parallel} \rangle < 0$. For the situations investigated here, we observe that this procedure works quite well, and the constraint violation $(1 - |\langle \mathcal{P} \rangle|^2)/L$ is consistent of the order of magnitude of machine precision.

In order to speed up the optimization, it is natural to contract \tilde{H} into a single MPO. For the purely local Hamiltonian, as in Eq. (1), the bond dimension is 2. The bond dimension of these MPOs can be reduced down to 4

(single constraint) and 6 (double constraint) by removing identical rows⁶¹. This can be also checked by performing an SVD decomposition of the MPO⁶². As an additional improvement, it is convenient to block two or three sites together into a single tensor, depending on the projector. By imposing the constraint on this new block, the number of local physical states is d=3 in the case of the single constraint with a 2-sites-block and d=4 in the case of the double constraint with a 3-sites block.

- ¹ T. Lahaye, C. Menotti, L. Santos, M. Lewenstein, and T. Pfau, Rep. Prog. Phys. **72**, 126401 (2009), 0905.0386.
- ² M. a. Baranov, M. Dalmonte, G. Pupillo, and P. Zoller, Chem. Rev. **112**, 5012 (2012).
- ³ R. Blatt and C. Roos, Nature Physics 8, 277 (2012).
- ⁴ L. D. Carr, D. DeMille, R. V. Krems, and J. Ye, New J. Phys. 11, 055049 (2009), 0904.3175.
- M. Saffman, T. G. Walker, and K. Molmer, Rev. Mod. Phys. 82, 2313 (2010), 0909.4777.
- ⁶ R. Löw, H. Weimer, J. Nipper, J. B. Balewski, B. Butscher, H. P. Büchler, and T. Pfau, Journal of Physics B: Atomic, Molecular and Optical Physics 45, 113001 (2012).
- ⁷ J. Lim, H.-g. Lee, and J. Ahn, Journal of the Korean Physical Society **63**, 867 (2013).
- ⁸ M. P. A. Jones, L. G. Marcassa, and J. P. Shaffer, Journal of Physics B: Atomic, Molecular and Optical Physics 50, 060202 (2017).
- ⁹ O. Morsch and I. Lesanovsky, Rivista del Nuovo Cimento 41(7), pp. 383-414 (2018).
- ¹⁰ S. de Léséleuc, V. Lienhard, P. Scholl, D. Barredo, S. Weber, N. Lang, H. P. Büchler, T. Lahaye, and A. Browaeys, .
- H. Bernien, S. Schwartz, A. Keesling, H. Levine, A. Omran, H. Pichler, S. Choi, A. S. Zibrov, M. Endres, M. Greiner, V. Vuletić, and M. D. Lukin, Nature **551**, 579 EP (2017).
- J. Zeiher, R. van Bijnen, P. Schauß, S. Hild, J. yoon Choi, T. Pohl, I. Bloch, and C. Gross, Nature Physics 12, 1095 (2016).
- ¹³ Y.-Y. Jau, A. M. Hankin, T. Keating, I. H. Deutsch, and G. W. Biedermann, Nature Physics **12**, 71 (2015).
- ¹⁴ R. Faoro, C. Simonelli, M. Archimi, G. Masella, M. M. Valado, E. Arimondo, R. Mannella, D. Ciampini, and O. Morsch, Phys. Rev. A 93, 030701 (2016).
- A. Keesling, A. Omran, H. Levine, H. Bernien, H. Pichler, S. Choi, R. Samajdar, S. Schwartz, P. Silvi, S. Sachdev, P. Zoller, M. Endres, M. Greiner, V. Vuletic, and M. D. Lukin, arXiv:1809.05540.
- ¹⁶ I. Bloch, J. Dalibard, and S. Nascimbène, Nat. Phys. 8, 267 (2012).
- ¹⁷ P. Fendley, K. Sengupta, and S. Sachdev, Phys. Rev. B 69, 075106 (2004).
- ¹⁸ R. Ghosh, A. Sen, and K. Sengupta, Phys. Rev. B **97**, 014309 (2018).
- ¹⁹ R. Samajdar, S. Choi, H. Pichler, M. D. Lukin, and S. Sachdev, Phys. Rev. A **98**, 023614 (2018).
- ²⁰ N. Chepiga and F. Mila, Phys. Rev. Lett. **122**, 017205 (2019).
- ²¹ S. Whitsitt, R. Samajdar, and S. Sachdev, Phys. Rev. B

- **98**, 205118 (2018), 1808.07056.
- 22 N. Chepiga and F. Mila, arxiv.1809.00746.
- P. Di Francesco, P. Mathieu, and D. Senechal, Conformal Field Theory, Graduate Texts in Contemporary Physics (Springer-Verlag, New York, 1997).
- ²⁴ M. Henkel, (1999), 10.1007/978-3-662-03937-3.
- ²⁵ D. A. Huse and M. E. Fisher, Phys. Rev. B **29**, 239 (1984).
- A. O. Gogolin, A. A. Nersesyan, and A. M. Tsvelik, Bosonization and strongly correlated systems (Cambridge University Press, Cambridge, 1998).
- N. V. Prokof'ev, B. V. Svistunov, and I. S. Tupitsyn, Journal of Experimental and Theoretical Physics 87, 310 (1998).
- ²⁸ S. R. White, Phys. Rev. Lett. **69**, 2863 (1992).
- ²⁹ T. F. Gallagher, <u>Rydberg Atoms</u>, Cambridge Monographs on Atomic, Molecular and Chemical Physics (CUP, 2005).
- ³⁰ M. D. Lukin, M. Fleischhauer, and R. Cote, Phys. Rev. Lett. 87, 1 (2001).
- ³¹ R. Baxter, Exactly Solved Models in Statistical Mechanics, Dover books on physics (Dover Publications, 2007).
- ³² V. L. Pokrovsky and A. L. Talapov, Phys. Rev. Lett. 42, 65 (1979).
- ³³ J. Sólyom and P. Pfeuty, Phys. Rev. B **24**, 218 (1981).
- ³⁴ G. von Gehlen, V. Rittenberg, and T. Vescan, Journal of Physics A: Mathematical and General **20**, 2577 (1987).
- ³⁵ G. von Gehlen and V. Rittenberg, Journal of Physics A: Mathematical and General 19, L625 (1986).
- ³⁶ V. Dotsenko, Nuclear Physics B **235**, 54 (1984).
- ³⁷ A. Osterloh, L. Amico, G. Falci, and R. Fazio, Nature 416, 608 EP (2002).
- ³⁸ L. Amico, R. Fazio, A. Osterloh, and V. Vedral, Rev. Mod. Phys. **80**, 517 (2008).
- ³⁹ S.-J. Gu, Int. J. Mod. Phys. B 24, 4371(2010) (2008), 0811.3127.
- ⁴⁰ P. Zanardi and N. Paunković, Phys. Rev. E **74**, 031123 (2006).
- ⁴¹ W.-L. You, Y.-W. Li, and S.-J. Gu, Phys. Rev. E **76**, 022101 (2007).
- ⁴² D. Schwandt, F. Alet, and S. Capponi, Phys. Rev. Lett. 103, 170501 (2009).
- A. F. Albuquerque, F. Alet, C. Sire, and S. Capponi, Phys. Rev. B 81, 064418 (2010).
- ⁴⁴ P. Calabrese and J. Cardy, Journal of Physics A: Mathematical and Theoretical 42, 504005 (2009).
- ⁴⁵ M. B. Plenio and S. Virmani, Quant.Inf.Comput. 7, 1 (2007).
- Since the Hilbert space is not a product of single-site Hilbert spaces, in order to compute the reduced density matrix we simply plunge back the ground state of the system

- into the full Hilbert $(\mathbb{C}^2)^{\otimes L}$.
- ⁴⁷ A. Läuchli and C. Kollath, J. Stat. **Mech.**, P05018 (2008).
- ⁴⁸ M. Dalmonte, W. Lechner, Z. Cai, M. Mattioli, A. M. Läuchli, and G. Pupillo, Phys. Rev. B **92**, 045106 (2015).
- ⁴⁹ A. B. Zamolodchikov, JETP Lett. **43**, 730 (1986), [Pisma Zh. Eksp. Teor. Fiz.43,565(1986)].
- ⁵⁰ Note that, in the k=0 sector, we have not split the spectra according to their reflection symmetry, since the latter seemed not to correspond to charge conjugation symmetry of the two charged sectors.
- ⁵¹ The full symmetry group of the Potts model is the permutation group $S_3 = \mathbb{Z}_3 \times \mathbb{Z}_2$. However, the \mathbb{Z}_2 symmetry generator leaves invariant only \mathbb{Z}_3 neutral states, namely the ones labeled by Q = 0. Thus the Q = 0 sector splits into two subsectors labeled by a \mathbb{Z}_2 quantum number. Since this will not be necessary to identify gaps with operator, it will not be used in the text.
- ⁵² F. Woynarovich and H. P. Eckle, Journal of Physics A: Mathematical and General 20, L443 (1987).
- ⁵³ G. Sun, A. K. Kolezhuk, and T. Vekua, Phys. Rev. B **91**,

- 014418 (2015).
- ⁵⁴ M. P. A. Fisher, P. B. Weichman, G. Grinstein, and D. S. Fisher, Phys. Rev. B **40**, 546 (1989).
- ⁵⁵ T. Mishra, J. Carrasquilla, and M. Rigol, Phys. Rev. B 84, 115135 (2011).
- ⁵⁶ M. Dalmonte, J. Carrasquilla, L. Taddia, E. Ercolessi, and M. Rigol, Phys. Rev. B 91, 165136 (2015).
- ⁵⁷ L. Wang, K. S. D. Beach, and A. W. Sandvik, Phys. Rev. B **73**, 014431 (2006).
- These confidence intervals only indicate the error in the fit; the same applies to the DMRG estimate of the same quantities.
- ⁵⁹ G. M. Crosswhite and D. Bacon, Phys. Rev. A **78**, 012356 (2008).
- ⁶⁰ Y. Zhuang, H. J. Changlani, N. M. Tubman, and T. L. Hughes, Phys. Rev. B **92**, 035154 (2015).
- ⁶¹ C. Hubig, I. P. McCulloch, and U. Schollwöck, Phys. Rev. B 95, 035129 (2017).
- ⁶² U. Schollwöck, Annals of Physics 326, 96 (2011), January 2011 Special Issue.